

Article

Magnetic Resonance Imaging of Methane Hydrate Formation and Dissociation in Sandstone with Dual Water Saturation

Stian Almenningen ^{1,*} , Per Fotland ² and Geir Ersland ¹¹ Department of Physics and Technology, University of Bergen, 5007 Bergen, Norway² Equinor ASA, 5020 Bergen, Norway

* Correspondence: stian.almenningen@uib.no

Received: 9 July 2019; Accepted: 19 August 2019; Published: 22 August 2019



Abstract: This paper reports formation and dissociation patterns of methane hydrate in sandstone. Magnetic resonance imaging spatially resolved hydrate growth patterns and liberation of water during dissociation. A stacked core set-up using Bentheim sandstone with dual water saturation was designed to investigate the effect of initial water saturation on hydrate phase transitions. The growth of methane hydrate ($P = 8.3$ MPa, $T = 1\text{--}3$ °C) was more prominent in high water saturation regions and resulted in a heterogeneous hydrate saturation controlled by the initial water distribution. The change in transverse relaxation time constant, T_2 , was spatially mapped during growth and showed different response depending on the initial water saturation. T_2 decreased significantly during growth in high water saturation regions and remained unchanged during growth in low water saturation regions. Pressure depletion from one end of the core induced a hydrate dissociation front starting at the depletion side and moving through the core as production continued. The final saturation of water after hydrate dissociation was more uniform than the initial water saturation, demonstrating the significant redistribution of water that will take place during methane gas production from a hydrate reservoir.

Keywords: methane hydrates in sandstone; phase transitions; magnetic resonance imaging

1. Introduction

Natural gas hydrates are crystalline compounds consisting of structured water stabilized by guest molecules. In nature, methane is the typical hydrate former and subsurface methane hydrates constitute a currently untapped global energy resource. The estimates of methane bound in hydrates vary between 10^{14} and 10^{18} m³ at STP [1], where around 99% of the hydrates exist in submarine sediments [2]. Several short-term field pilots have been undertaken to prove the concept of methane gas production from methane hydrates: depressurization and associated hydrate dissociation onshore [3], depressurization offshore [4], and CO₂ injection and subsequent methane production onshore [5]. Important parameters for all production schemes are the hydrate saturation and distribution within the pore space. The hydrate, water, and gas saturation in the reservoir govern the rate of methane recovery during depressurization-induced hydrate dissociation [6]. Understanding the growth pattern of methane hydrate within pores is thus considered important to be able to predict the production response in different hydrate accumulations based on the local saturation distribution.

Magnetic resonance imaging (MRI) is a powerful tool to characterize natural sediments [7] and to measure and visualize flow and reactions in porous media [8–10]. MRI is based on aligning nuclear spins, usually hydrogen-nuclei, in a magnetic field and recording the response of the nuclei as they are exposed to radiofrequency pulses. The recorded response is used to map the amount of nuclei

inside the porous media. The non-invasive imaging technique is particularly useful for hydrate phase transitions in sedimentary core plugs. The spin-spin relaxation of hydrogen-nuclei in liquid water is slower than the relaxation of hydrogen-nuclei in solid hydrates, making the liquid water detectable during MR scans, in contrast to solid hydrates. The onset of hydrate formation is detected as a loss of signal when liquid water converts to hydrates, and hydrate dissociation is recognized as a signal increase when liquid water re-appears during hydrate dissociation. This technique has previously been reported to track the amount of water in sediments both spatially and temporally during hydrate growth and dissociation [11–13]. MRI has also been used to prove the concept of CO₂–CH₄ exchange when methane hydrate in sandstone is exposed to CO₂ [8,14].

This paper reports the spatial growth pattern of methane hydrates in sandstone cores at sub-cm scale. A dual water saturation system created by aligning two cores with different initial water saturation was used to identify the effect of water saturation. MRI spatially visualized methane hydrate growth and subsequent hydrate dissociation with respect to initial water saturation. Interpretation of T_2 measurements during hydrate phase transitions improved the understanding of hydrate growth and dissociation patterns at pore-scale.

2. Materials and Methods

2.1. Experimental Set-Up

Cylindrical Bentheim sandstone cores with an average porosity and permeability of 22–24% and 1–2 D, respectively, were used as host sediment for the hydrate phase transitions. The sandstone was fairly clean and consisted of around 96% quartz sand [15]. The specialized core holder was made from polyether ether ketone (PEEK) and titanium materials to ensure the compatibility with the MR instrument (Figure 1). Floating end-pieces (PEEK) were positioned on each side of the core inside a rubber sleeve and uniaxial core confinement was provided by pressurized fluorinert (liquid containing no hydrogen). Both flow lines leading into the core were connected to a high-pressure, high-precision pump (Quizix Q6000, Chandler Engineering, Tulsa, USA), which controlled the pore pressure. A custom-made cooling jacket was fitted around the core holder and the temperature was regulated by throughput of precooled air. A temperature sensor (TMQIN-062U-12, Omega, Manchester, United Kingdom) located in the confining fluorinert next to the inlet end-piece monitored the system temperature. The entire core holder was placed inside the MR instrument for real-time image acquisition. The superconductive magnet (BioSpec 47/40 USR, Bruker, Rheinstetten, Germany) had a magnetic field strength of 4.7 T (200 MHz) and could accommodate cylindrical core holders with diameters up to 19 cm. The longitudinal field of view limited the total length of the cores to 12 cm.

2.2. Experimental Procedure

Two cylindrical core samples with equal diameters of 6.31 cm and lengths of 7.93 and 3.93 cm were stacked and mounted in the core holder (Figure 2). In the first experiment (Exp. 1), the short core was completely saturated by 0.1 wt% NaCl brine and the long core was dry (air-filled). In the second experiment (Exp. 2), the cores were reassembled with opposite saturation with the long core completely saturated by brine, while the short core remained dry. However, the dry core was partly saturated with brine in both of the experiments when the cores were mounted in the core holder. Spontaneous imbibition and compression by the confining pressure moved some water from the wet core into the dry core. The resulting stacked cores acted as a composite core with dual water saturation (Figure 2), enabling investigation of the effect of initial water saturation on methane hydrate growth. One pump filled with water (0.1 wt% NaCl) was connected to the water-filled core, whereas another pump filled with methane gas provided pressure control to the low water saturation core. The pore pressure was subsequently increased to 8.30 MPa by injecting gas from one side, while the effective overburden pressure was continuously kept at 3.00 MPa. The system was left for five days to saturate the pore water completely with dissolved methane.

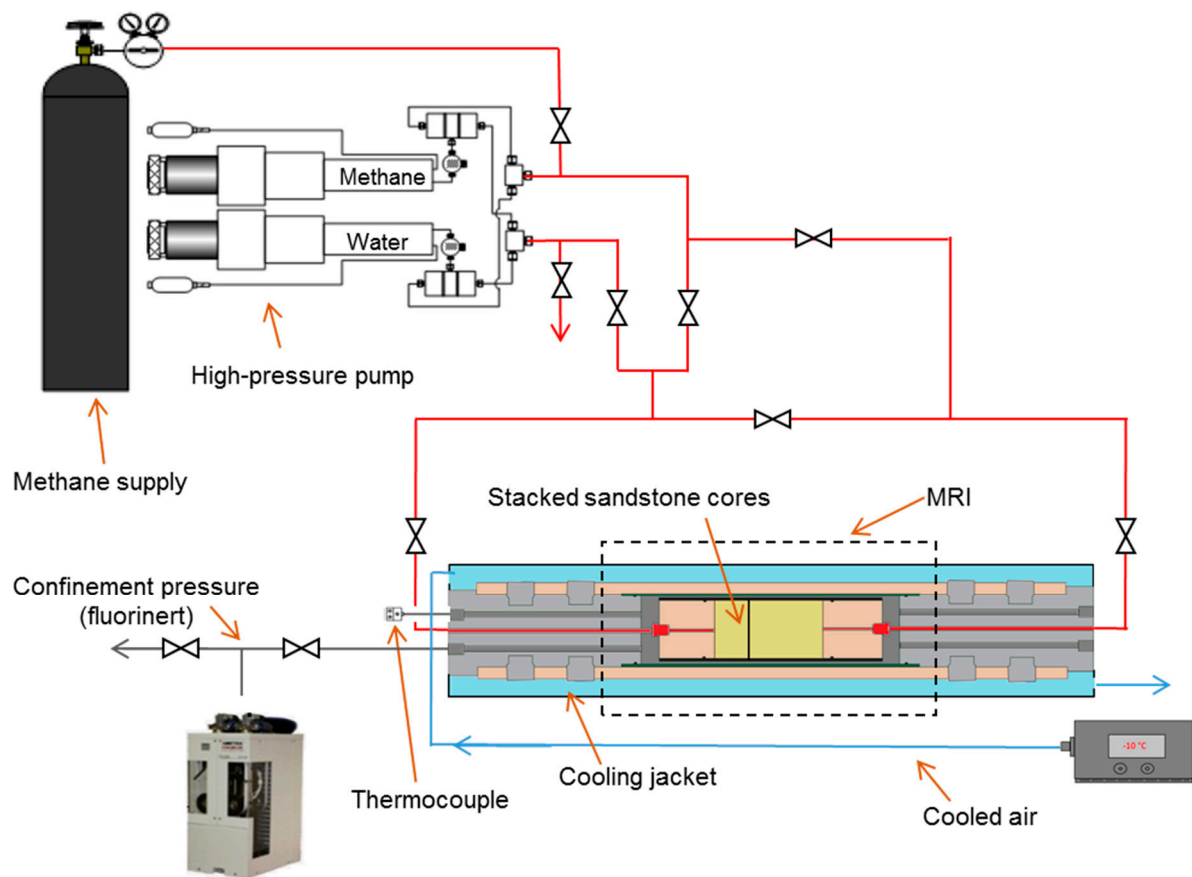


Figure 1. Schematic of experimental set-up. High-pressure flow lines for methane gas and water in red, cooled air for temperature control in light blue, and pressurized fluorinert for confinement pressure in gray.

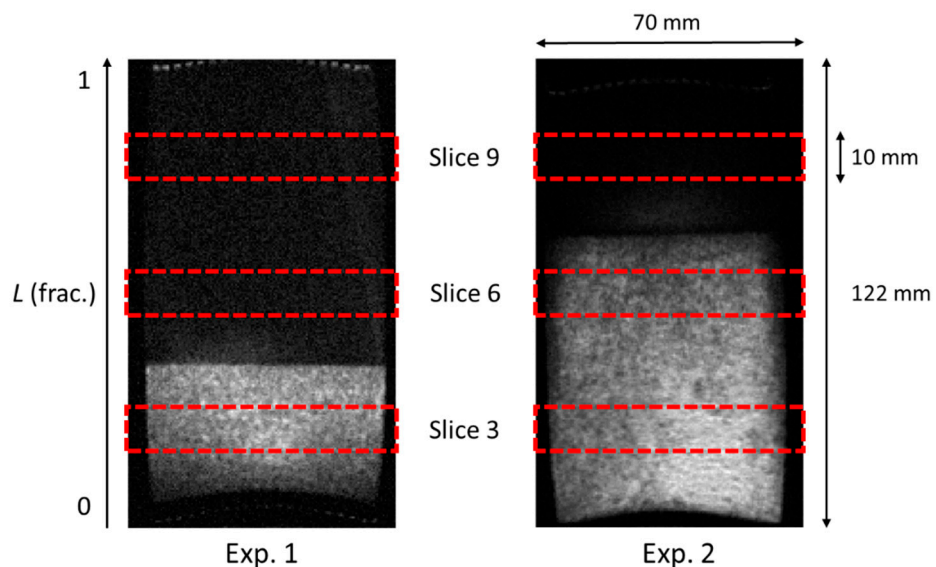


Figure 2. Sagittal view of the initial water saturation in the composite core. Exp. 1 (left) started with a short water-filled core stacked together with a long air-filled core. Exp. 2 (right) started with the opposite saturation in the cores. The red dashed rectangles mark the position of the three axial slices that are used to visualize hydrate growth throughout the results section.

Hydrate formation initiated after reducing the temperature to approximately 1–3 °C. The pore pressure remained constant at 8.30 MPa throughout the growth process, and the amount of methane gas consumed by hydrate formation determined the hydrate saturation. The change in water saturation was in sequence monitored by two different MR scan protocols: (1) The distribution of water was visualized and quantified by RAREst 2D scans (rapid acquisition with relaxation enhancement with short echo time). The echo time was set to 5.84 ms and the voxel resolution was $0.5 \times 0.5 \times 1.0$ mm. Twelve axial slices with a thickness of 10 mm and a slice gap of 0.5 mm covered the entire length of the composite core sample. A short scan time of 4 min 5 s was enabled by a Rare factor of two and no signal averaging. (2) The pore-scale water distribution measurements (T_2 mapping) were inferred by MSME 2D scans (multi slice-multi echo). An echo time of 6.25 ms was used with 100 echo images in each echo train. Axial slices with the same resolution as for the RAREst scans were used and the scan time was 17 min 39 s. The slices obtained by RAREst scans were cropped circularly with the same diameter as the core, and the average background noise was subtracted from the signal intensity of each voxel in the core. The water saturation was found by correlating the average signal intensity of the entire core with volume logs from the pump. Local hydrate saturation was calculated assuming changes in water saturation corresponded to hydrate growth and no redistribution of water between voxels. The MSME slices were cropped and an average T_2 decay curve was extracted from each cross-section of the core. Application of inverse Laplace transform converted the decay curve to a T_2 distribution curve. The local average T_2 value was calculated throughout the hydrate growth process.

Two different approaches were used to dissociate the hydrate in the two experiments. In Exp. 1, the gas permeability was nonzero after hydrate formation and the gas permeability was estimated by constant volumetric gas injection and application of Darcy's law. The pressure was then reduced from one side of the core by constant volumetric gas extraction (0.5 mL/min) until complete dissociation. In Exp. 2, the apparent gas permeability was zero, indicating complete blockage of pores. In this case, the pressure reduction was initiated from both ends of the core and the pressure was lowered until approximately 0.8 MPa above the dissociation pressure. Hydrate dissociation followed by constant volumetric gas production (1.0 mL/min) from one side of the core while monitoring the differential pressure across the core. The production pressure was later set constant to 4.00 MPa when the differential pressure reached 1.00 MPa, and was maintained constant throughout the rest of the dissociation process. The same MR scans as for hydrate formation were acquired during hydrate dissociation.

3. Results and Discussions

3.1. Intensity vs. Water Saturation

The signal intensity in each voxel obtained by the RAREst scan is a relative measure of the amount of liquid water in each voxel. However, spin-echo based sequences (e.g., RAREst) are sensitive to the applied echo time as the transverse relaxation of hydrogen-nuclei in liquid water residing close to solid grains may be too fast for signal capture. The effect is more prominent for high surface relaxivity (paramagnetic ions) and low water saturation in water-wet porous media as the surface-to-volume ratio increases. Additionally, the transverse relaxation is enhanced as the water molecules diffuse through internal gradients in the pores that arise from magnetic susceptibility differences between the water and solid grains [16]. The relationship between signal intensity and water saturation during hydrate growth was thus investigated, and is shown for both experiments in Figure 3. The average water saturation during hydrate growth was calculated based on the amount of consumed methane gas at a constant pressure [17]. A hydration number of 5.99 was used [18]. As seen from Figure 3, the measured signal intensity (average) deviates from the linear trend for water saturations lower than 0.5. A polynomial correlation (dotted lines) was used to estimate local water saturations.

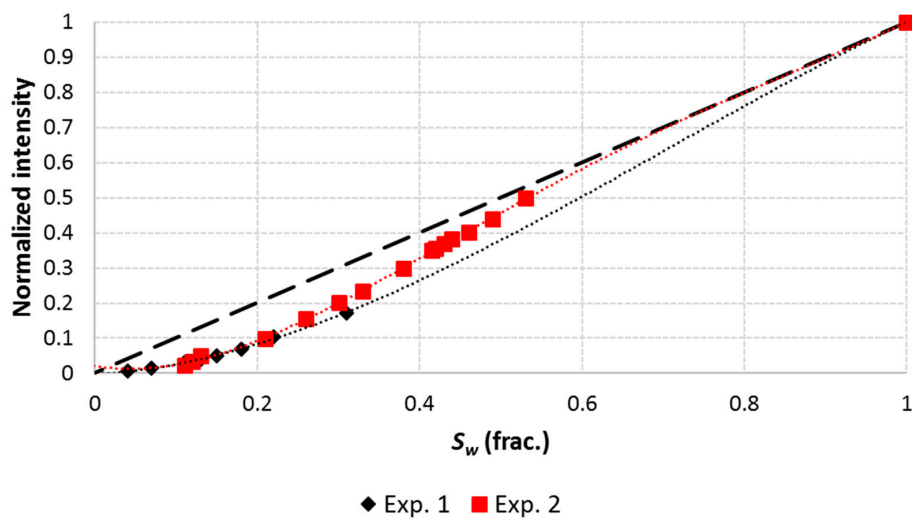


Figure 3. Correlation between average voxel intensity and average water saturation for both experiments. A linear trend line based on the end-point measurement ($S_w = 1$) is added for comparison. Notice that the measured intensity values are lower than the linear correlation for S_w of less than approximately 0.5.

3.2. Methane Hydrate Growth

The initial condition for the first experiment was a dual water saturation system where one-third of the composite sandstone core had high water saturation and two-thirds had low water saturation (detailed saturation in Figure 4). The methane hydrate growth initiated throughout the length of the core, but most of the hydrate formed in the high water saturation region. Here, the initial water saturation of 0.7 was converted to a hydrate saturation of 0.8 after three days of formation. During the same time, the low water saturation region ($S_w \approx 0.2$) yielded a final hydrate saturation of 0.1–0.2. Most of the pore water formed hydrate and a uniform water saturation of less than 0.1 remained after formation. The high degree of water conversion to hydrate is believed to be facilitated by a combination of the following: (1) The initial saturation of 0.7 water and 0.3 methane gas ensured a large interfacial area between water and gas. Methane gas, being the non-wetting phase, was distributed as connected channels in the middle of the pore space. The large interface between water and gas promoted methane diffusion into the water phase and provided an extensive interfacial area for nucleation of hydrate. (2) The effect of salt inhibition during hydrate growth was minor because the initial water salinity was only 0.1 wt% NaCl.

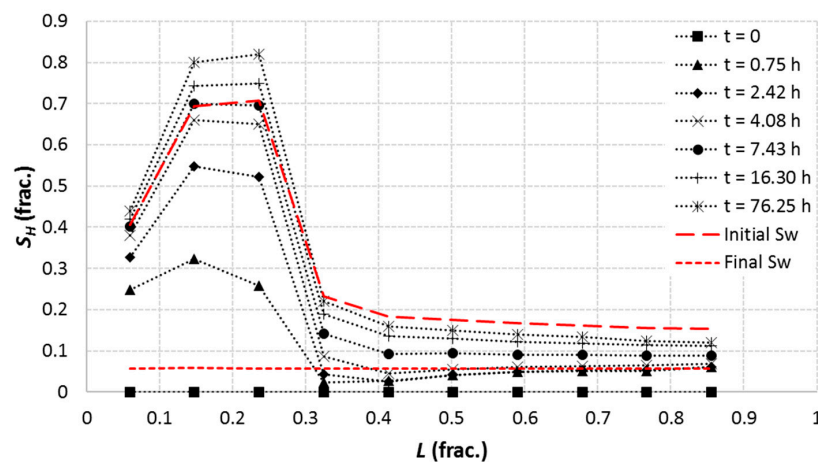


Figure 4. Methane hydrate saturation profiles during hydrate growth in Exp. 1. The pressure and temperature were kept constant at 8.30 ± 0.03 MPa and 2.3 ± 0.5 °C, respectively.

Axial imaging of the core revealed that the initial water saturation was distributed in transverse bands in the high water saturation region as a result of laminations in the Bentheim sandstone (Figure 5). These high water saturation bands likely reflected areas with smaller pore sizes than the adjacent areas where the water was displaced by gas. The initial fast hydrate growth in these bands containing tighter pores is similar to the increased growth rate observed for smaller grain sizes [11,19]. Preferred formation of hydrate in high water saturation regions was also observed by Seol & Kneafsey [20]. The nature of nucleation and number of nucleation sites [19] was not resolved with the sampling frequency used. However, the hydrate growth was not observed to propagate like a front in either of the directions, which have been observed previously [13].

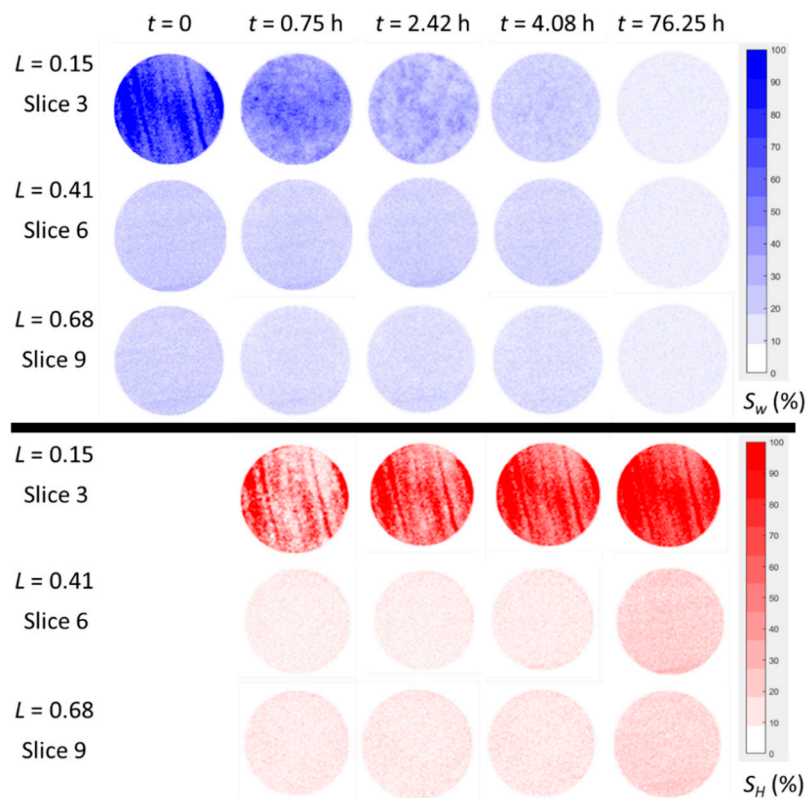


Figure 5. Water distribution (top) and methane hydrate distribution (bottom) in three different cross-sections of the composite core during hydrate growth in Exp. 1. The pressure and temperature were kept constant at 8.30 ± 0.03 MPa and 2.3 ± 0.5 °C, respectively.

The initial water saturation in Exp. 2 was close to unity in one end of the composite core and decreasing towards 0.1–0.2 in the other end (Figure 6). The resulting hydrate saturation followed the same distribution and decreased from 0.9 to 0 along the length of the core. The local amount of water limited the final amount of hydrate that was generated, similar to that observed in Exp. 1. The overall hydrate formation ceased at a uniform water saturation of around 0.1. The growth of hydrate in the low water saturation region ($L > 0.65$) started after more than one day of growth in the high water saturation region ($L < 0.65$). The trend was that the growth of hydrate started and continued in the high water saturation region until the water saturation dropped to similar values as in the low water saturation region. At this point, the hydrate growth also started in the low water saturation region. The location of water in relation to the grain surfaces may affect the hydrate formation and will be discussed later in this section. The formation of hydrate was faster in the high water saturation areas within each cross-section of the core (Figure 7). However, the growth pattern had no clear direction within the high water saturation areas, for example, radially inwards from the core perimeter or from one side to the other [12]. The growth pattern was spatially heterogeneous, as observed by Bagherzadeh et al. [19].

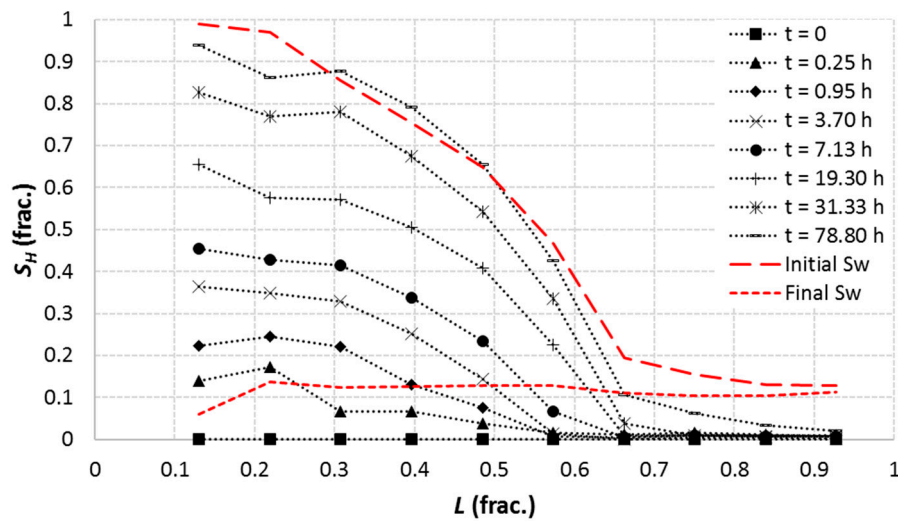


Figure 6. Methane hydrate saturation profiles during hydrate growth in Exp. 2. The pressure and temperature were kept constant at 8.30 ± 0.03 MPa and 3 ± 1 °C, respectively.

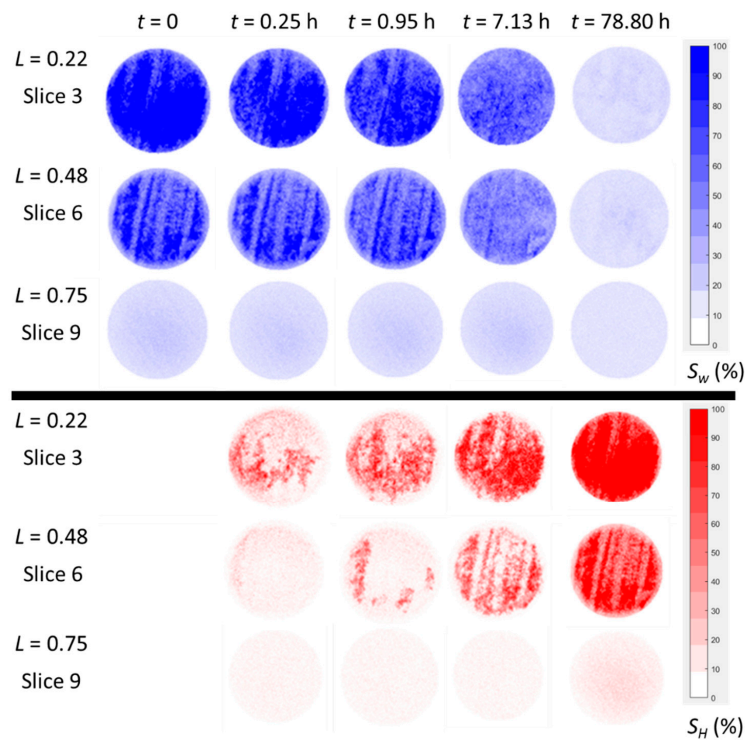


Figure 7. Water distribution (**top**) and methane hydrate distribution (**bottom**) in three different cross-sections of the composite core during hydrate growth in Exp. 2. The pressure and temperature were kept constant at 8.30 ± 0.03 MPa and 3 ± 1 °C, respectively.

The different saturation regions yielded different T_2 distribution curves, as the area under the T_2 distribution curve for a given slice is proportional to the water saturation in that slice (Figure 8). In addition, the response of the average T_2 was clearly different for the high- and low-saturation regions (Figures 9 and 10). The average T_2 was initially high and decreased nearly linearly with the increase in hydrate saturation as hydrate formed in the high water saturation regions. The reduction in average T_2 implies that the surface-to-volume ratio of the liquid water increased, which would be the result independent of how the hydrate nucleated in a water-filled pore. Nucleation in the middle of the pore or at the grain surface would both lead to an increase of the surface-to-volume ratio. However,

the rapid decline in average T_2 suggests that the hydrate formed in the middle of the pores in the high water saturation regions. The same decrease in average T_2 was not observed for the low water saturation regions, where the initial average T_2 already was low as a result of water residing at the grain surfaces (Figures 9 and 10). Here, the limited amount of hydrate growth was accompanied with an unaltered average T_2 value. Pore-scale methane hydrate growth has previously been shown to follow the gas–water interface in an excess gas system [21]. A similar growth pattern here was probably the reason that only small amounts of hydrate formed in the low water saturation regions. Thin layers of hydrate formed between gas occupying the center of pores and water residing close to grains. The average T_2 ended at approximately the same value (5–10 ms) throughout the whole core after hydrate formation independent of the initial water saturation. This implies that the amount and configuration of remaining water were the same after hydrate formation in regions with both high and low initial water saturation. The only difference between the regions was the extent to which the rest of the pore space was filled with hydrate compared with gas. In either way, the remaining water was likely bound to the grain surfaces and could not convert to hydrate because of the low activity associated with bound water [22] and/or lack of methane supply. In another study, a submicron to micron thick water film was always present between gas hydrate and the hydrophilic quartz surface [23].

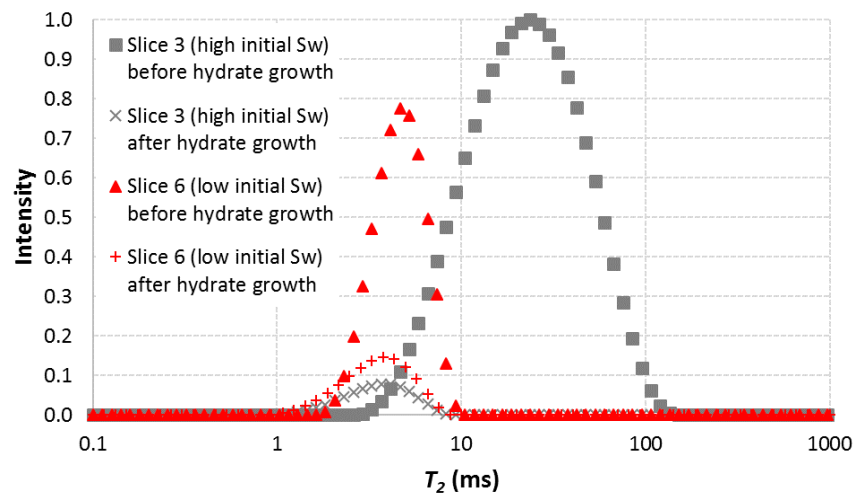


Figure 8. Distribution of transverse relaxation time constant, T_2 , for Exp. 1. In slice 3 (high initial S_w), the intensity of the distribution decreases and shifts leftwards as the hydrate grows. The intensity of the distribution in slice 6 (low initial S_w) decreases as the hydrate grows, but the average T_2 remains constant.

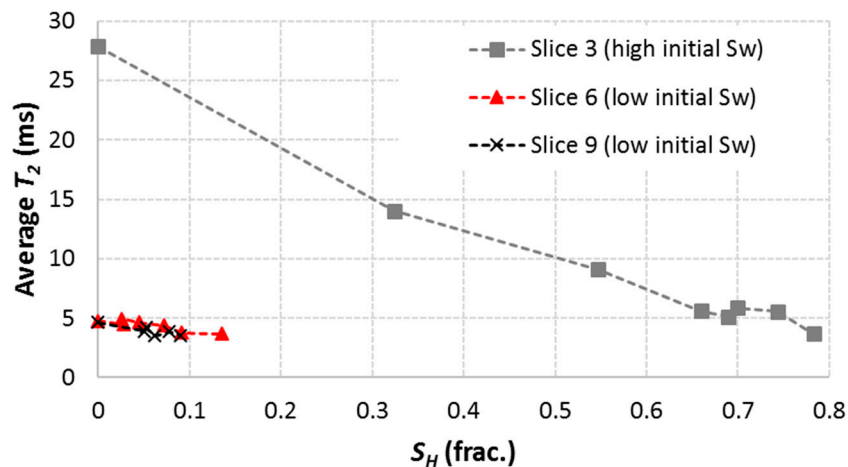


Figure 9. Average T_2 in three different cross-sections of the core during hydrate growth in Exp. 1.

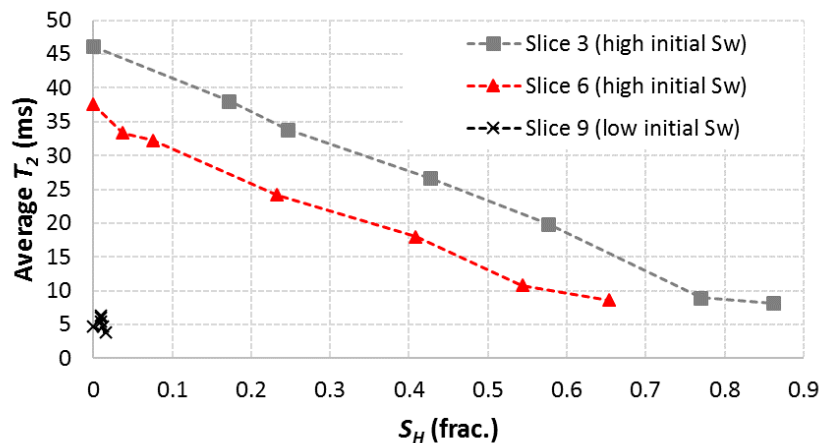


Figure 10. Average T_2 in three different cross-sections of the core during hydrate growth in Exp. 2.

3.3. Methane Hydrate Dissociation

The permeability of the core in Exp. 1 was significantly reduced after hydrate formation and the effective gas permeability was measured to 0.8 mD. In comparison, the absolute permeability of Bentheim sandstone is 1–2 D. The relatively low, but significant permeability suggests that the pressure reduction transmitted throughout the core during gas production from one side, that is, no differential pressure was introduced across the core during the production period. Producing gas with constant volumetric flow rate of 0.5 mL/min triggered hydrate dissociation at the production side ($L = 1$) when the pressure reached 3.74 MPa (Figure 11). The dissociation started at the production side and propagated through the core as a front, even though the differential pressure was zero. It should be noted that the cooling of the core holder was configured in a way that introduced the cooling medium (air) into the cooling jacket at $L = 0$, and then it flowed along the length of the core holder and exited at $L = 1$. This cooling set-up would induce a minor temperature gradient along the length of the core. The start of the hydrate dissociation at the production side may thus be a result of a slightly elevated temperature compared to the far (cooler) end of the core. The initial dissociation at $P = 3.74$ MPa implies that the temperature was 3.6 °C based on the stability pressure of methane hydrate [24], which is close to the 3.0 ± 0.6 °C that was measured in the confining liquid during the dissociation process. The dissociation pattern within each axial slice was also different from the observed hydrate growth pattern (Figure 12). The dissociation seemed to start at one place and then spread transversally from there.

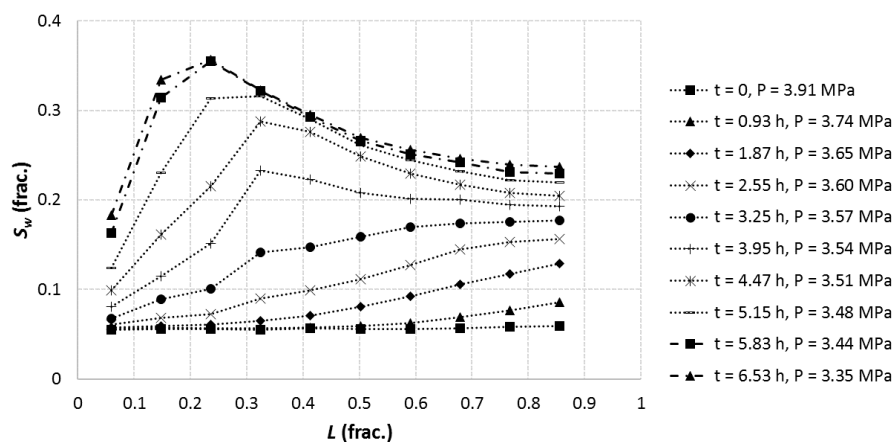


Figure 11. Water saturation profiles during hydrate dissociation in Exp. 1. Methane gas was produced with constant volumetric flow rate of 0.5 mL/min. The change in production pressure with time is denoted in the legend. Temperature was kept constant at 3.0 ± 0.6 °C.

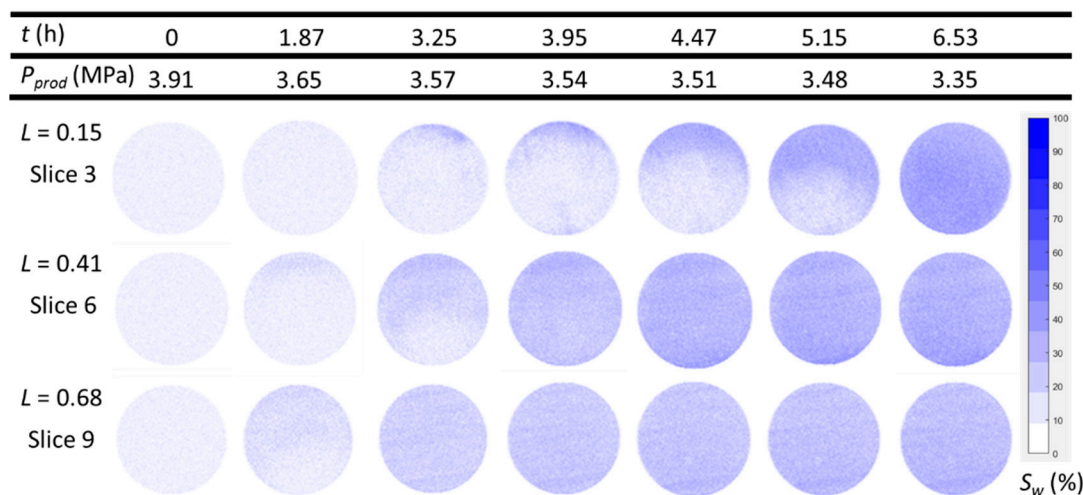


Figure 12. Water distribution in three different cross-sections of the core during hydrate dissociation in Exp. 1. Methane gas was produced with constant volumetric flow rate of 0.5 mL/min. The change in production pressure with time is denoted in the heading. Temperature was kept constant at 3.0 ± 0.6 °C.

Explicit mapping of the hydrate saturation was not possible during dissociation, in contrast to the growth process. The quantification of hydrate saturation during formation was based on the premise that all reduction in water saturation corresponded to formation of hydrate, not because of flow of water inside the core. This assumption is reasonable for hydrate growth at a constant pressure, but not for gas production at a constant flow rate. The final average water saturation after complete dissociation was 0.27 compared with the initial water saturation before hydrate formation, which was 0.31. Furthermore, 13% of the water originally in place was produced (into tubing) during the dissociation process.

Production of gas from one side of the core in Exp. 2 caused an immediate build-up of differential pressure across the core, and the effective gas permeability could not be measured. The average saturation of gas after hydrate formation was 0.36, contrary to Exp. 1 where the average gas saturation was 0.61. In some cross-sections of the core ($L < 0.3$), the gas saturation was close to zero. The pressure was thus reduced to 5.00 MPa from both ends of the core. The production of methane gas was then started by a constant volumetric flow rate of 1.0 mL/min from one side of the core ($L = 1$), and hydrate dissociation was triggered at the production side when the pressure reached 4.17 MPa (Figure 13). The dissociation front moved from the production side towards the other end of the core ($L = 0$). At the time when the production pressure reached 4.00 MPa and was set to a constant pressure, a differential pressure of 1.00 MPa was obtained and sustained while the hydrate continued to dissociate. The gas permeability of the core became measurable again three hours later when the dissociation front reached the end of the core ($t = 3.70$ h, Figure 13). The slow hydrate dissociation in the region with highest hydrate saturation ($L < 0.3$) demonstrates the impact of hydrate and gas saturation on the rate of methane recovery [6]. The dissociation was finished after approximately ten hours and left the core with an average water saturation of 0.30. Furthermore, 43% of the water originally in place was produced during the dissociation process.

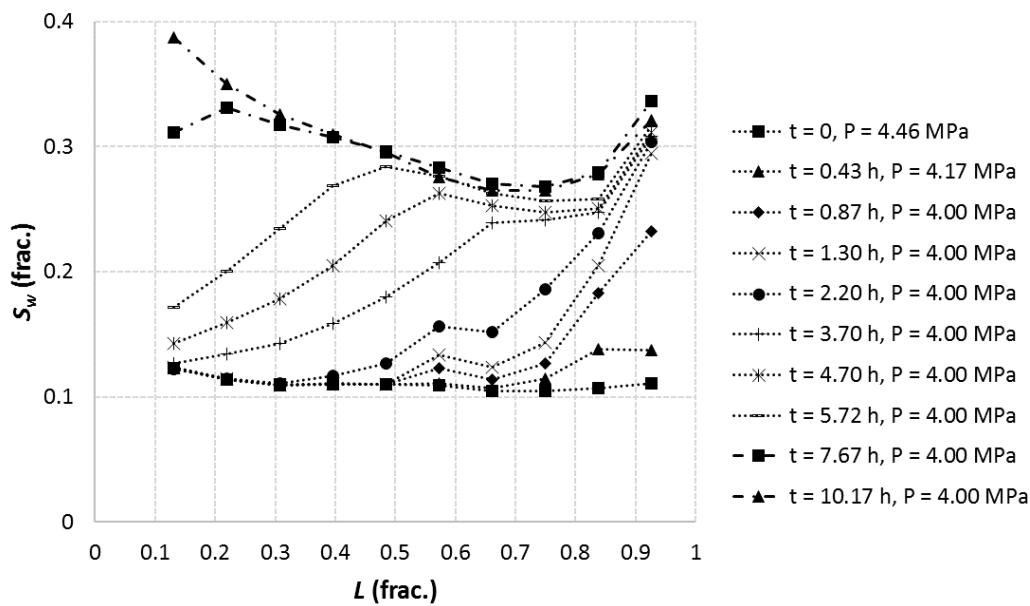


Figure 13. Water saturation profiles during hydrate dissociation in Exp. 2. Methane gas was initially produced with constant volumetric flow rate of 1.0 mL/min. The production pressure was set to constant when the pressure reached 4.00 MPa. Temperature was kept constant at 4.2 ± 0.5 °C.

The dissociation seemed to start at the perimeter of the core and proceeded radially inwards to the core center (Figure 14), similar to the pattern that was observed for thermally-induced hydrate dissociation [19]. The effect of heat transfer from the boundary of the core is believed to dictate the dissociation pattern. Gas expansion during production causes a depression of the core temperature. The temperature drop is less at the perimeter of the core close to the surrounding temperature control, contrary to the center of the core where the temperature drop is largest. The resulting temperature gradient with slightly elevated temperature at the perimeter of the core causes the hydrate dissociation to start at the boundary; for example, slice 9, Figure 14.

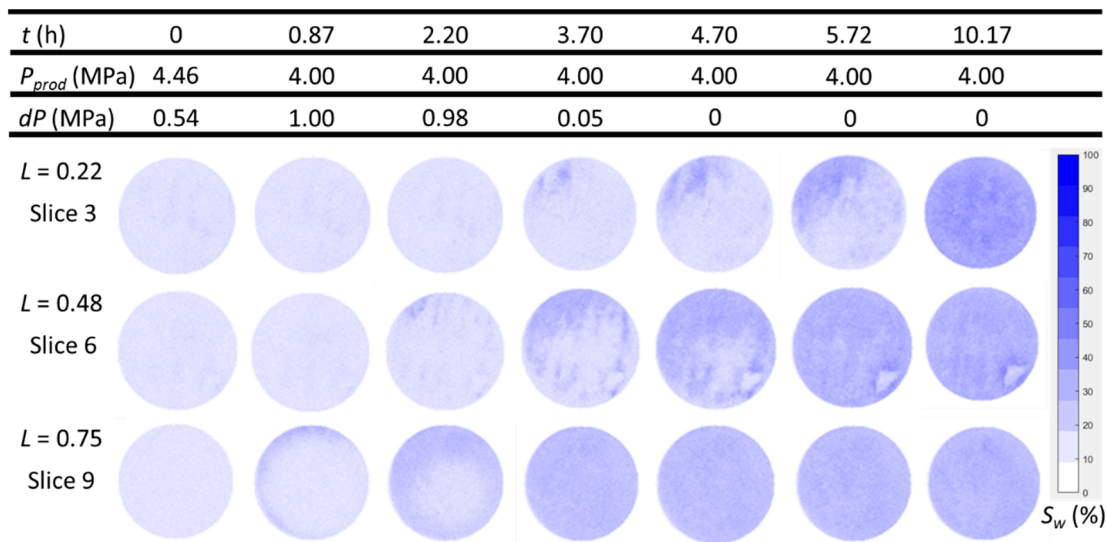


Figure 14. Water distribution in three different cross-sections of the core during hydrate dissociation in Exp. 2. Methane gas was initially produced with constant volumetric flow rate of 1.0 mL/min. The production pressure was set to constant when the pressure reached 4.00 MPa. The change in production pressure and differential pressure across the length of the core are denoted in the heading. Temperature was kept constant at 4.2 ± 0.5 °C.

The dissociation of hydrate was accompanied by an increase in average T_2 for every cross-section of the core in both experiments (Figures 15 and 16). The magnitude of the average T_2 was mainly a function of water saturation and was independent of the longitudinal location in the core. This means that the liberated water during dissociation had approximately the same surface-to-volume ratio throughout the length of the core. The water that was not produced out from the core during dissociation distributed itself towards pore walls with gas residing in the middle of the pores, giving a more uniform saturation of gas and water than prior to the hydrate formation. The formation and subsequent dissociation of hydrate is clearly an effective method to homogenize the fluid saturation in a core sample with heterogeneous initial fluid saturation.

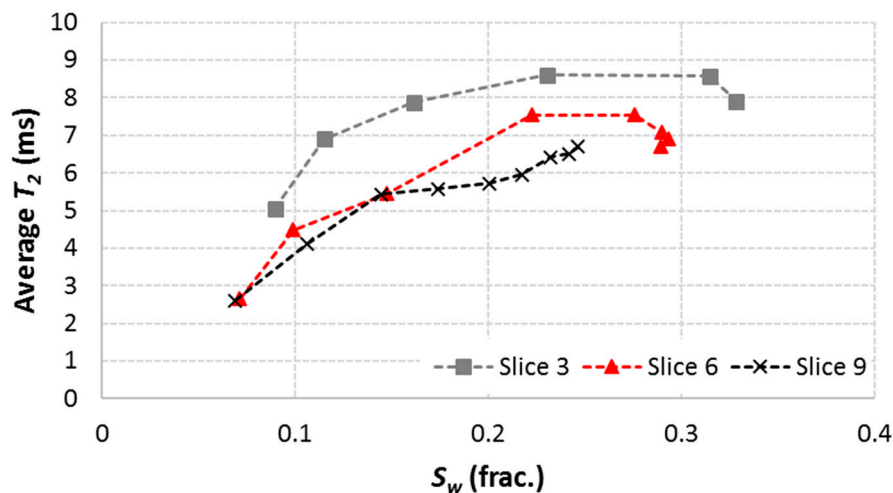


Figure 15. Average T_2 in three different cross-sections of the core during hydrate dissociation in Exp. 1.

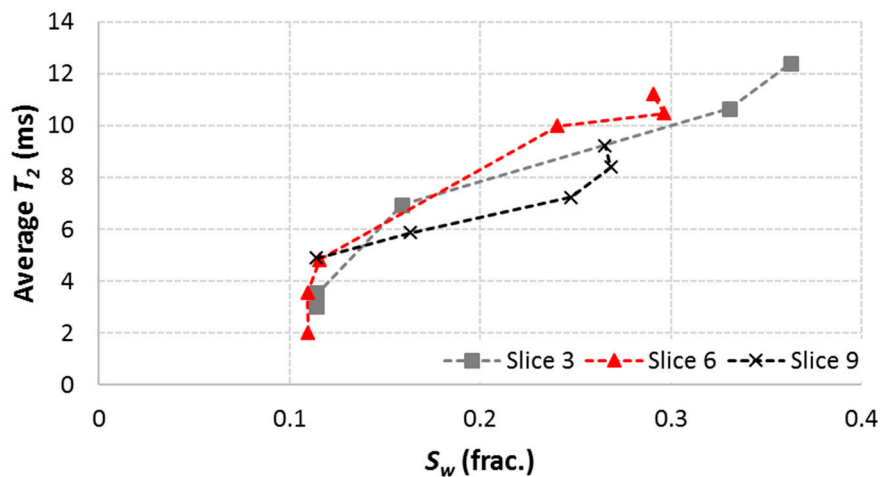


Figure 16. Average T_2 in three different cross-sections of the core during hydrate dissociation in Exp. 2.

4. Conclusions

Magnetic resonance imaging was successfully used to map the water saturation during methane hydrate formation and dissociation in Bentheim sandstone cores. The visualization showed that the growth of hydrate was more prominent in regions of the core with high water saturation. The final hydrate distribution was controlled by the initial water distribution, giving a uniform remaining water saturation of around 0.1 after hydrate formation. The average transverse relaxation time constant, T_2 , decreased significantly during growth in high water saturation regions and remained unchanged during limited growth in low water saturation regions. Pressure depletion from one end of the core led to a dissociation front starting at the production side and moving through the length of the core.

The concomitant flow of water and gas during dissociation led to a final water saturation that was more uniform than the initial water saturation.

Author Contributions: Conceptualization, S.A., P.F. and G.E.; methodology, S.A., P.F. and G.E.; software, S.A., P.F. and G.E.; validation, S.A., P.F. and G.E.; formal analysis, S.A.; investigation, S.A.; resources, S.A., P.F. and G.E.; data curation, S.A., P.F. and G.E.; writing—original draft preparation, S.A.; writing—review and editing, S.A., P.F. and G.E.; visualization, S.A.; supervision, P.F. and G.E.; project administration, P.F. and G.E.; funding acquisition, P.F. and G.E.

Funding: This research was funded by Equinor through the Academia Agreement with the University of Bergen, Norway.

Acknowledgments: The authors would like to acknowledge Equinor for financial support and the use of the MRI facility at Equinor's laboratories in Bergen, Norway.

Conflicts of Interest: The authors declare no conflict of interest.

References

1. Milkov, A.V. Global Estimates of Hydrate-Bound Gas in Marine Sediments: How Much Is Really Out There? *Earth-Sci. Rev.* **2004**, *66*, 183–197. [[CrossRef](#)]
2. Ruppel, C.D.; Kessler, J.D. The Interaction of Climate Change and Methane Hydrates. *Rev. Geophys.* **2017**, *55*, 126–168.
3. Kurihara, M.; Sato, A.; Funatsu, K.; Ouchi, H.; Yamamoto, K.; Numasawa, M.; Ebinuma, K.; Narita, H.; Masuda, Y.; Dallimore, S.; et al. Analysis of Production Data for 2007/2008 Mallik Gas Hydrate Production Tests in Canada. In Proceedings of the International Oil and Gas Conference and Exhibition, Beijing, China, 8–10 June 2010.
4. Konno, Y.; Fujii, T.; Sato, A.; Akamine, K.; Naiki, M.; Masuda, Y.; Yamamoto, K.; Nagao, J. Key Findings of the World's First Offshore Methane Hydrate Production Test off the Coast of Japan: Toward Future Commercial Production. *Energy Fuels* **2017**, *31*, 2607–2616. [[CrossRef](#)]
5. Schoderbek, D.; Martin, K.L.; Howard, J.J.; Silpngarm, S.; Hester, K. North Slope Hydrate Fieldtrial: CO₂/CH₄ Exchange. In Proceedings of the OTC Arctic Technology Conference, Houston, TX, USA, 3–5 December 2012.
6. Almendinger, S.; Fotland, P.; Fernø, M.A.; Ersland, G. An Experimental Investigation of Gas-Production Rates During Depressurization of Sedimentary Methane Hydrates. *SPE J.* **2019**, *24*, 522–530. [[CrossRef](#)]
7. Kleinhans, M.G.; Jeukens, C.R.L.P.N.; Bakker, C.J.G.; Frings, R.M. Magnetic Resonance Imaging of Coarse Sediment. *Sediment. Geol.* **2008**, *208*, 69–78. [[CrossRef](#)]
8. Ersland, G.; Husebø, J.; Graue, A.; Baldwin, B.A.; Howard, J.J.; Stevens, J. Measuring Gas Hydrate Formation and Exchange with CO₂ in Bentheim Sandstone Using MRI Tomography. *Chem. Eng. J.* **2010**, *158*, 25–31. [[CrossRef](#)]
9. Fernø, M.A.; Haugen, Å.; Wickramathilaka, S.; Howard, J.J.; Graue, A.; Mason, G.; Morrow, N.R. Magnetic Resonance Imaging of the Development of Fronts During Spontaneous Imbibition. *J. Petrol. Sci. Eng.* **2013**, *101*, 1–11.
10. Oswald, S.E.; Spiegel, M.A.; Kinzelbach, W. Three-Dimensional Saltwater-Freshwater Fingering in Porous Media: Contrast Agent MRI as Basis for Numerical Simulations. *Magn. Reson. Imaging* **2007**, *25*, 537–540. [[CrossRef](#)] [[PubMed](#)]
11. Zhao, J.; Lv, Q.; Li, Y.; Yang, M.; Liu, W.; Yao, L.; Wang, S.; Zhang, Y.; Song, Y. In-Situ Visual Observation for the Formation and Dissociation of Methane Hydrates in Porous Media by Magnetic Resonance Imaging. *Magn. Reson. Imaging* **2015**, *33*, 485–490. [[CrossRef](#)] [[PubMed](#)]
12. Baldwin, B.A.; Moradi-Araghi, A.; Stevens, J. Monitoring Hydrate Formation and Dissociation in Sandstone and Bulk with Magnetic Resonance Imaging. *Magn. Reson. Imaging* **2003**, *21*, 1061–1069. [[CrossRef](#)] [[PubMed](#)]
13. Baldwin, B.A.; Stevens, J.; Howard, J.J.; Graue, A.; Kvamme, B.; Aspenes, E.; Ersland, G.; Husebø, J.; Zornesb, D.R. Using Magnetic Resonance Imaging to Monitor CH₄ Hydrate Formation and Spontaneous Conversion of CH₄ Hydrate to CO₂ Hydrate in Porous Media. *Magn. Reson. Imaging* **2009**, *27*, 720–726. [[CrossRef](#)] [[PubMed](#)]

14. Graue, A.; Kvamme, B.; Baldwin, B.; Stevens, J.; Howard, J.J.; Aspenes, E.; Ersland, G.; Husebo, J.; Zornes, D. MRI Visualization of Spontaneous Methane Production From Hydrates in Sandstone Core Plugs When Exposed to CO₂. *SPE J.* **2008**, *13*, 146–152. [[CrossRef](#)]
15. Ramstad, T.; Rueslåtten, H. *Pore Scale Numerical Analysis for Geological Sequestration of CO₂*; Technical Report from Task 1, 1–63; Numerical Rocks: Trondheim, Norway, 2013.
16. Mitchell, J.; Chandrasekera, T.C.; Johns, M.L.; Gladden, L.F.; Fordham, E.J. Nuclear Magnetic Resonance Relaxation and Diffusion in the Presence of Internal Gradients: The Effect of Magnetic Field Strength. *Phys. Rev. E* **2010**, *81*, 026101. [[CrossRef](#)] [[PubMed](#)]
17. Almennigen, S.; Flatlandsmo, J.; Fernø, M.A.; Ersland, G. Multiscale Laboratory Verification of Depressurization for Production of Sedimentary Methane Hydrates. *SPE J.* **2017**, *22*, 138–147. [[CrossRef](#)]
18. Circone, S.; Kirby, S.H.; Stern, L.A. Direct Measurement of Methane Hydrate Composition along the Hydrate Equilibrium Boundary. *J. Phys. Chem. B* **2005**, *109*, 9468–9475. [[CrossRef](#)] [[PubMed](#)]
19. Bagherzadeh, S.A.; Moudrakovski, I.L.; Ripmeester, J.A.; Englezos, P. Magnetic Resonance Imaging of Gas Hydrate Formation in a Bed of Silica Sand Particles. *Energy Fuels* **2011**, *25*, 3083–3092. [[CrossRef](#)]
20. Seol, Y.; Kneafsey, T.J. Methane Hydrate Induced Permeability Modification for Multiphase Flow in Unsaturated Porous Media. *J. Geophys. Res. Solid Earth* **2011**, *116*, 1–15. [[CrossRef](#)]
21. Almennigen, S.; Iden, E.; Fernø, M.A.; Ersland, G. Salinity Effects on Pore-Scale Methane Gas Hydrate Dissociation. *J. Geophys. Res. Solid Earth* **2018**, *123*, 5599–5608. [[CrossRef](#)]
22. Clennell, M.B.; Hovland, M.; Booth, J.S.; Henry, P.; Winters, W.J. Formation of Natural Gas Hydrates in Marine Sediments: 1. Conceptual Model of Gas Hydrate Growth Conditioned by Host Sediment Properties. *J. Geophys. Res. Solid Earth* **1999**, *104*, 22985–23003.
23. Chaouachi, M.; Falenty, A.; Sell, K.; Enzmann, F.; Kersten, M.; Haberthür, D.; Kuhs, W.F. Microstructural Evolution of Gas Hydrates in Sedimentary Matrices Observed with Synchrotron X-Ray Computed Tomographic Microscopy. *Geochem. Geophys.* **2015**, *16*, 1711–1722. [[CrossRef](#)]
24. Colorado School of Mines. Center for Hydrate Research. 2015. Available online: <http://hydrates.mines.edu/CHR/Software.html> (accessed on 2 March 2016).



© 2019 by the authors. Licensee MDPI, Basel, Switzerland. This article is an open access article distributed under the terms and conditions of the Creative Commons Attribution (CC BY) license (<http://creativecommons.org/licenses/by/4.0/>).